The Astrophysical Journal Letters, 926:L29 (6pp), 2022 February 20 https://doi.org/10.3847/2041-8213/ac51dd
© 2022. The Author(s). Published by the American Astronomical Society.
OPEN ACCESS

Thermal Instability–Induced Fundamental Magnetic Field Strands in the Solar Corona

Patrick Antolin[1], Juan Martínez-Sykora[2,3,4,5], and Seray Şahin[1]
[1] Department of Mathematics, Physics and Electrical Engineering, Northumbria University, Newcastle upon Tyne, NE1 8ST, UK; patrick.antolin@northumbria.ac.uk
[2] Lockheed Martin Solar & Astrophysics Laboratory, 3251 Hanover Street, Palo Alto, CA 94304, USA
[3] Bay Area Environmental Research Institute, NASA Research Park, Moffett Field, CA 94035, USA
[4] Rosseland Centre for Solar Physics, University of Oslo, PO Box 1029 Blindern, NO-0315 Oslo, Norway
[5] Institute of Theoretical Astrophysics, University of Oslo, PO Box 1029 Blindern, NO-0315 Oslo, Norway
Received 2022 January 6; revised 2022 February 4; accepted 2022 February 4; published 2022 February 22

Abstract

Thermal instability is a fundamental process of astrophysical plasmas. It is expected to occur whenever the cooling is dominated by radiation and cannot be compensated for by heating. In this work, we conduct 2.5D radiation MHD simulations with the *Bifrost* code of an enhanced activity network in the solar atmosphere. Coronal loops are produced self-consistently, mainly through Joule heating, which is sufficiently stratified and symmetric to produce thermal nonequilibrium. During the cooling and driven by thermal instability, coronal rain is produced along the loops. Due to flux freezing, the catastrophic cooling process leading to a rain clump produces a local enhancement of the magnetic field, thereby generating a distinct magnetic strand within the loop up to a few Gauss stronger than the surrounding coronal field. These strands, which can be considered fundamental, are a few hundred kilometers in width, span most of the loop leg, and emit strongly in the UV and extreme UV (EUV), thereby establishing a link between the commonly seen rain strands in the visible spectrum with the observed EUV coronal strands at high resolution. The compression downstream leads to an increase in temperature that generates a plume-like structure, a strongly emitting spicule-like feature, and short-lived brightening in the UV during the rain impact, providing an explanation for similar phenomena seen with IRIS. Thermal instability and nonequilibrium can therefore be associated with localized and intermittent UV brightening in the transition region and chromosphere, as well as contribute to the characteristic filamentary morphology of the solar corona in the EUV.

Unified Astronomy Thesaurus concepts: Plasma astrophysics (1261); Solar corona (1483); Solar coronal loops (1485); Radiative magnetohydrodynamics (2009); Solar coronal waves (1995); Solar magnetic fields (1503); Magnetohydrodynamical simulations (1966); Solar prominences (1519)

Supporting material: animations

1. Introduction

Coronal rain is a catastrophic cooling phenomenon that is commonly seen in quiescent active region loops (Schrijver 2001; Antolin & Rouppe van der Voort 2012) and flare loops during their cooling phase (Jing et al. 2016; Scullion et al. 2016). Recently, this phenomenon has also been reported in the quiet Sun, forming in magnetic dips associated with null point topologies (Schad et al. 2016; Li et al. 2018; Mason et al. 2019; Chen et al. 2021). Cool and dense, partially ionized plasma is observed to appear within minutes in the UV and visible wavelengths and fall along loop-like structures at velocities much lower than freefall (De Groof et al. 2004). The field-aligned morphology is often clumpy and compact in chromospheric wavelengths such as Hα and more elongated (and therefore more continuous) in transition region (TR) lines such as Si IV 1402 Å (Antolin et al. 2015). In the cross-field direction, the rain often appears multistranded with typical sizes of 100–300 km (Antolin & Rouppe van der Voort 2012; Jing et al. 2016). Such sizes are very similar to the high-resolution observations of coronal strands in the extreme UV (EUV) with *Hi-C* (Brooks et al. 2013; Aschwanden & Peter 2017; Williams et al. 2020), and a possible reason for this common ground may reside in the sizes involved in the granular motion and the associated currents, as described by Martínez-Sykora et al. (2018). The observed velocities are broad but usually reach above 100 km s^{-1} prior to impact in the chromosphere that can be supersonic (Kleint et al. 2014; Straus et al. 2015). Their kinetic energies are large enough to cause short-lived or sustained UV brightening events (Kleint et al. 2014; Chitta et al. 2016; Chen et al. 2021), depending on the downflowing mass flux.

Coronal rain events are usually associated with regions that exhibit a significant change in intensity across the EUV spectrum. Long-period intensity pulsations are a clear example of such variability (Froment et al. 2015), which is strongly associated with coronal rain (Antolin 2020). When observed on-disk, the supersonic downflows often occur along plume-like structures rooted in sunspot umbrae or penumbrae (Dere 1982; Brynildsen et al. 2001; Nelson et al. 2020). Besides being more dynamic at TR wavelengths, such regions also show a puzzling significant change in morphology when observed at cooler EUV wavelengths, appearing more filamentary (Kjeldseth-Moe & Brekke 1998; Ugarte-Urra et al. 2009).

The quiescent coronal rain kind is now understood as being part of thermal nonequilibrium (TNE) cycles that are produced because of strongly stratified heating. The TNE scenario satisfactorily explains the long-period intensity pulsations and periodic coronal rain (Froment et al. 2017; Auchère et al. 2018). Klimchuk & Luna (2019) provided an analytical description of the TNE conditions and predicted that apex-to-

Original content from this work may be used under the terms of the Creative Commons Attribution 4.0 licence. Any further distribution of this work must maintain attribution to the author(s) and the title of the work, journal citation and DOI.

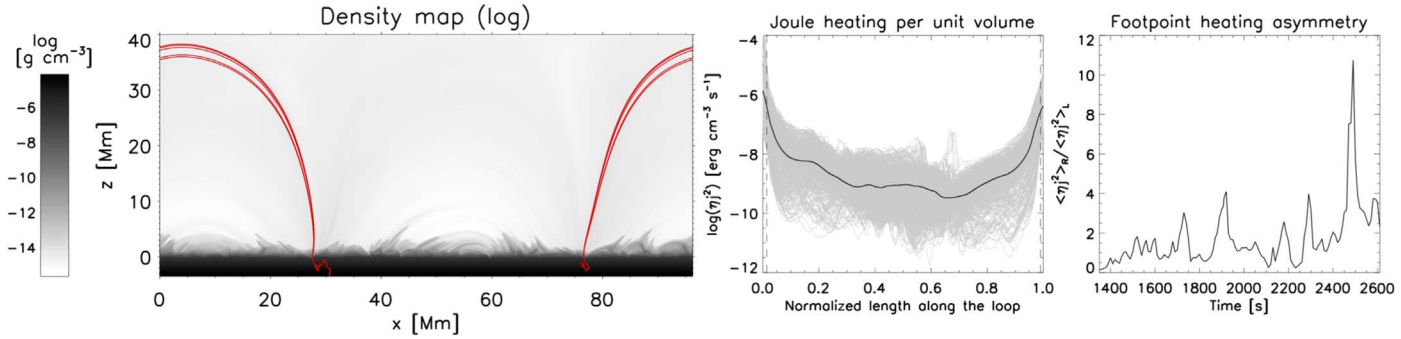

Figure 1. Density map (left) in the numerical domain, Joule heating per unit volume (middle), and footpoint heating asymmetry (right) along a thermally unstable loop. The red lines indicate selected magnetic field lines intersecting the region where coronal rain forms. The middle panel shows the Joule heating per unit volume profiles along the red field lines for all the time steps (in gray) and the average (in black). The TR location at each footpoint is indicated by dashed vertical lines. The right panel shows the ratio of the Joule heating per unit volume between the right and left footpoints (as seen in the left panel), averaged over 10% of the loop length from the TR upward.

footpoint heating below 0.1 is a necessary condition, which can be sufficient if heating asymmetry between both footpoints is not large. During the gradual cooling stage of a TNE cycle, thermal instability (TI) can occur, which is thought to be the driver behind the formation of the condensations that compose coronal rain (Field 1965; Claes & Keppens 2021). The shear flows produced by the gas pressure loss from TI (Fang et al. 2015), combined with pressure redistribution across loops due to the strong density change (Oliver et al. 2014), are thought to be behind the rain morphology and lower-than-freefall dynamics (Li et al. 2021). Recently, 3D MHD modeling of coronal rain was achieved (Moschou et al. 2015; Xia et al. 2017), including the first radiative-MHD (rMHD) modeling with self-consistent coronal rain formation (Kohutova et al. 2020), in which the heating is produced through magnetoconvective motions and associated processes. However, such large-scale simulations fail to achieve the required resolution to properly characterize the morphology and its observational signatures. For more detail on the TNE–TI interplay, see the recent review by P. Antolin & C. Froment (2022, in preparation).

In this work, we conduct 2.5D rMHD simulations at high resolution with *Bifrost* (Gudiksen et al. 2011) of a large-scale numerical box modeling enhanced solar activity network, self-consistently heated through magnetoconvection (Section 2). We show for the first time (Section 3) that the TI process of coronal rain formation can significantly enhance the magnetic field strength locally to create strands, thereby establishing a link with the observed EUV coronal strands. We further show the influence in morphology in the EUV and UV wavelengths that this process has. Discussion and conclusions are presented in Section 4.

2. Model

We used the 2.5D rMHD numerical simulation described in detail in Martínez-Sykora et al. (2017) but for later instances when the coronal rain started to form. The simulation has been calculated with the 3D rMHD *Bifrost* code (Gudiksen et al. 2011). The computed radiation in the photosphere and lower chromosphere is optically thick, including scattering (Skartlien 2000; Hayek et al. 2010). Radiative losses and gains in the upper chromosphere and TR through recipes are derived from detailed non-LTE calculations using RADYN (Carlsson & Leenaarts 2012). Optically thin radiative losses in the corona are based on Chianti emissivities (e.g., Del Zanna et al. 2021). The model also includes field-aligned thermal conduction.

The simulated region spans 90 Mm horizontally and ranges from 3 Mm below to 40 Mm above the surface. The horizontal resolution is uniform with a 14 km grid spacing, while the vertical resolution is nonuniform with the highest resolution in the photosphere, chromosphere, and TR (∼12 km grid spacing). The magnetic field configuration includes two plage regions of opposite polarity with an unsigned mean magnetic field of ∼190 G (Figure 1).

The boundary conditions are periodic in the horizontal direction and open in the vertical direction. The bottom boundary has a constant entropy in inflow regions to maintain the solar convective motions with ∼5780 K effective temperature at the photosphere. See Martínez-Sykora et al. (2017) for further details.

3. Results

The numerical model is characterized by self-consistent heating produced by the magnetoconvective motions in the subphotosphere, which energize the magnetic field lines in the upper atmosphere. The *Bifrost* atmospheres are known to be heated primarily by Joule heating (Kanella & Gudiksen 2019), with it being concentrated in the upper transition and lower corona (Gudiksen & Nordlund 2005; Hansteen et al. 2010). Recent 3D rMHD simulations with *Bifrost* show that such footpoint-concentrated heating can lead to coronal rain (Kohutova et al. 2020).

Advancing on previous models, the current simulation significantly increases the spatial resolution while self-consistently producing coronal loops. In addition, the numerical box is larger, allowing an extended coronal region with longer coronal loops. The Joule heating per unit volume along multiple field lines of a particular loop with rain is shown in the middle panel of Figure 1. It decreases exponentially with height, with the ratio of heating between the apex and the low corona well below 0.1, on average. Moreover, the heating asymmetry between both footpoints is mostly below 3, except when the clump impacts the chromosphere (right panel of Figure 1). These are the main ingredients for the onset of TNE (Klimchuk & Luna 2019).

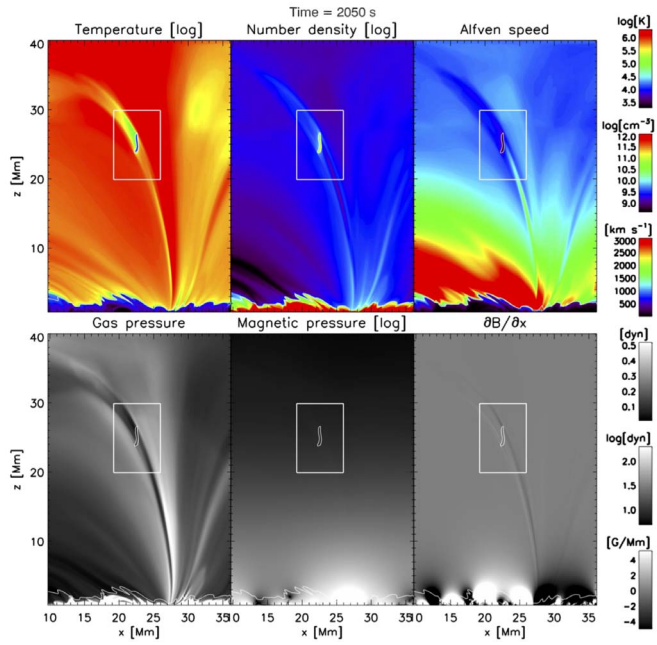

Figure 2. Thermodynamic and magnetic structure of the thermally unstable loop. From top to bottom and left to right, respectively, we have the temperature (log), density (log), Alfvén speed, gas pressure, magnetic pressure, and derivative of the magnetic field strength with respect to x, for a snapshot of the simulation at a time in which the coronal rain clump has formed. The white square denotes the zoomed-in region shown in Figure 3. The accompanying animation shows the evolution of the loop over the time span of 25 minutes, from formation in the corona to impact in the lower atmosphere. The real-time animation duration is 14 s.

(An animation of this figure is available.)

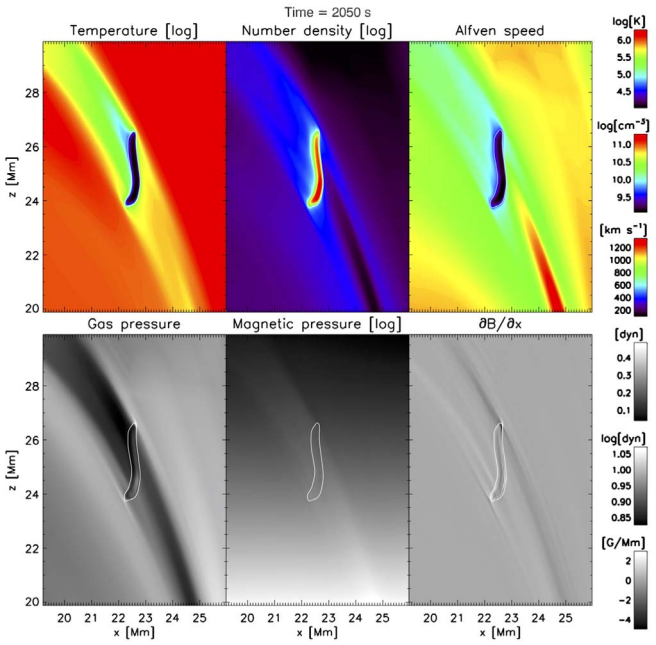

Figure 3. Zoomed-in snapshot of the thermodynamic and magnetic structure of a rain clump. Following the layout in Figure 2, the region shown here corresponds to the white square inset in that figure. The accompanying animation corresponds to the same interval as in Figure 2. The real-time animation duration is 14 s.

(An animation of this figure is available.)

3.1. Magnetic Field and Thermodynamic Variation

Changes in the connectivity of an open field region are seen at $t \approx 1000$ s after the start of the simulation, with various open field lines reconnecting and closing to form a long loop, which is shown in Figure 1 (see the associated animation). The region as a whole continuously cools, on average, irrespective of the topological change. Just over 10 minutes after the loop closing, catastrophic cooling occurs, accompanied by a local collapse of the gas pressure and the formation of a condensation near the loop apex, as seen in Figure 2.

The temperature at the location of rain formation drops exponentially from an average of 10^6 K to minima of $\approx 2 \times 10^5$ K at a rate of 500–1000 K s^{-1} (within 10 minutes) prior to rain appearance. The decrease then further accelerates to 2000–5000 K s^{-1} at the time of rain formation, down to 10^4 K within 30–60 s, which is characteristic of TI and matches observations (Antolin et al. 2015). The temperature in the clump then roughly stabilizes during the rest of the fall. The temperature drop is accompanied by a strong number density increase up to 10^{10}–10^{11} cm^{-3}, on average. The clump is at all times strongly multithermal and inhomogeneous, with a very cool and dense chromospheric core at 7000 K and 10^{12} cm^{-3} at the very tip (head) of the clump of only a few hundred kilometers in width and length and a warm elongated tail at $10^{4.2}$–$10^{4.5}$ K and number densities of $10^{10.5}$–$10^{11.2}$ cm^{-3}. The cross-field transition layer from the rain core to the external corona, known as the condensation–corona transition region (CCTR), is only on the order of 100 km. Such thermodynamic values and morphologies agree very well with coordinated SST-IRIS observations spanning chromospheric to TR temperatures (Antolin et al. 2015).

The loss of temperature and density increase are accompanied by a loss of gas pressure of ≈0.5 dyn across the loop. This variation is not confined to the clump's location but occurs along most of the loop due to the strong radiative losses and the advection of material that forms the clump. This global pressure loss advects the magnetic field lines inward (closer together) due to flux freezing, leading to the slight increase of magnetic pressure seen in Figures 2 and 3. The magnetic field strength increases by a few Gauss across the structure, which can be understood based on simple pressure balance conditions ($\frac{\Delta B^2}{8\pi} = \Delta p$).

Figure 4 shows time–distance diagrams for various heights for horizontal sections across the coronal structure. The location and time occurrence of the rain are shown to match well with the formation of a distinct magnetically enhanced region. The enhancement is seen to increase in time, and the width of the enhanced region matches well with the width of the rain at various heights.

3.2. Clump Alignment with the Field

The coronal rain clump undergoes strong deformation during the fall due to the shear flows and rapidly changing thermodynamic conditions downstream (Fang et al. 2015). The catastrophic cooling occurs quasi-simultaneously (within 1 minute) in multiple field lines spanning a maximum width of ≈3 Mm across and over a height span of ≈4 Mm. The elongated clump is therefore at first not aligned with the field. As it falls, different parts fall at different speeds, probably due to the variation in density across (effect described by Oliver et al. 2014; Martínez-Gómez et al. 2020) and also due to the shear flows. The overall cross-field width of the clump is

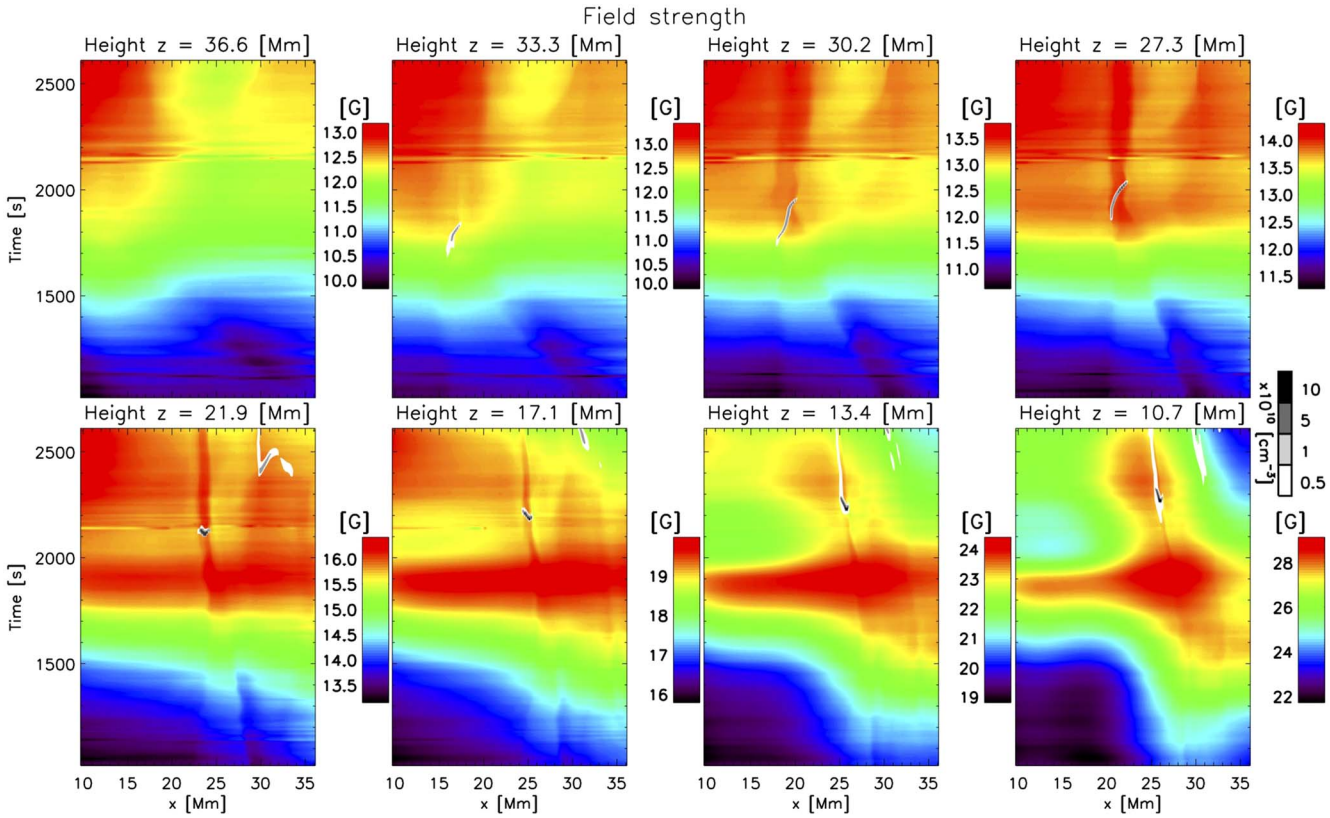

Figure 4. Magnetic field evolution with height for the region containing the thermally unstable loop. From top to bottom and left to right, we show time–distance maps at several heights of the magnetic field strength for a range along the *x*-axis containing the thermally unstable loop. We overlay in gray scale color density isocontours that capture the rain clump. The accompanying animation shows the change in height of this time–distance map, starting from a height of 40 Mm and ending at a height of 8.7 Mm. The real-time animation duration is 29 s.

(An animation of this figure is available.)

reduced due to the field area expansion with height. The length therefore changes strongly, decreasing to ≈1 Mm before elongating again in the last 20 Mm before impact, reaching 3–4 Mm in length, and only then aligning with the field.

When the rain clump stretches and aligns with the field in the last 20 Mm, the clump obtains its minimum width values, averaging 410 ± 120 km, with minima at the cool and dense tip of ≈130 km. The clump accelerates downward, reaching maximum speeds of 150 km s^{-1} at a height of 20 Mm. The Mach number $M = \frac{v_{\rm clump}}{c_{s,\rm down}}$, with $v_{\rm clump}$ the speed of the clump and $c_{s,\rm down}$ the sound speed in the corona, downstream of the clump, reaches values above 1 in the last 7 Mm. In the last 7 Mm, the clump undergoes strong deceleration to speeds of ≈70 km s^{-1} due to a large pressure increase to 2.3 dyn.

3.3. Filamentary Structure in TR Lines

Over the last 20 Mm before impact, the region downstream is strongly compressed, and while the temperature at the wake, within 20 Mm of the clump, is in the range $\log T = 5$–5.5, the temperature downstream increases to $\log T = 5.8$–5.9 due to the compression. At the same time, the number density in the downstream region increases from 2×10^9 to 2×10^{10} cm^{-3} just prior to impact. The conditions downstream of the rain are therefore perfect for TR line emission. In Figure 5, we show the synthesized emissivity in the Fe IX 171.073 and Si IV 1402.77 Å lines. As expected, the strongest emitting region in the Fe IX line is the region downstream of the rain clump, with the emissivity increasing over time as the clump gets closer to the chromosphere. Moreover, due to the elongated TR present along most of the loop leg (with the temperature dropping from $\log T = 6$ to $\log T = 5$–5.5 and the number density increasing from $10^{9.5}$ to $10^{9.8}$–10^{10} cm^{-3}), a strongly emitting sheath in Fe IX 171.073 Å forms at both sides of the clump. This strongly emitting region in the Fe IX line is strongly reminiscent of a plume with filamentary structure, as is often observed during supersonic downflow events associated with coronal rain (Nelson et al. 2020).

At the lower formation temperatures of the Si IV line, essentially the same cross-field width of the rain core is observed, reflecting the very thin CCTR enveloping the clump, still unresolved in observations (Antolin et al. 2015). The wake of the clump is a strongly emitting region during most of the fall, due to its high density and low temperature at $\log T \approx 5$. The emitting strand elongates continuously and is seen to be 40 Mm long (almost half the loop) at the end.

The structure of the multithermal loop emitting across chromospheric to EUV lines with an extended EUV emitting tail obtained in the simulation matches well with the observations, as shown in the composite image of the right panel of Figure 5, with AIA 171 (blue), IRIS/SJI 1400 (green), and 2796 (red). The clumpier morphology of coronal rain is lacking in this image, likely due to the relatively coarse resolution (0.″33 pixel size, ≈500 km resolution).

The strongest emitting region in the Si IV line (by 1–2 orders of magnitude compared to the tail) is the envelope of the clump and the immediate 1–2 Mm part of the tail, closely matching

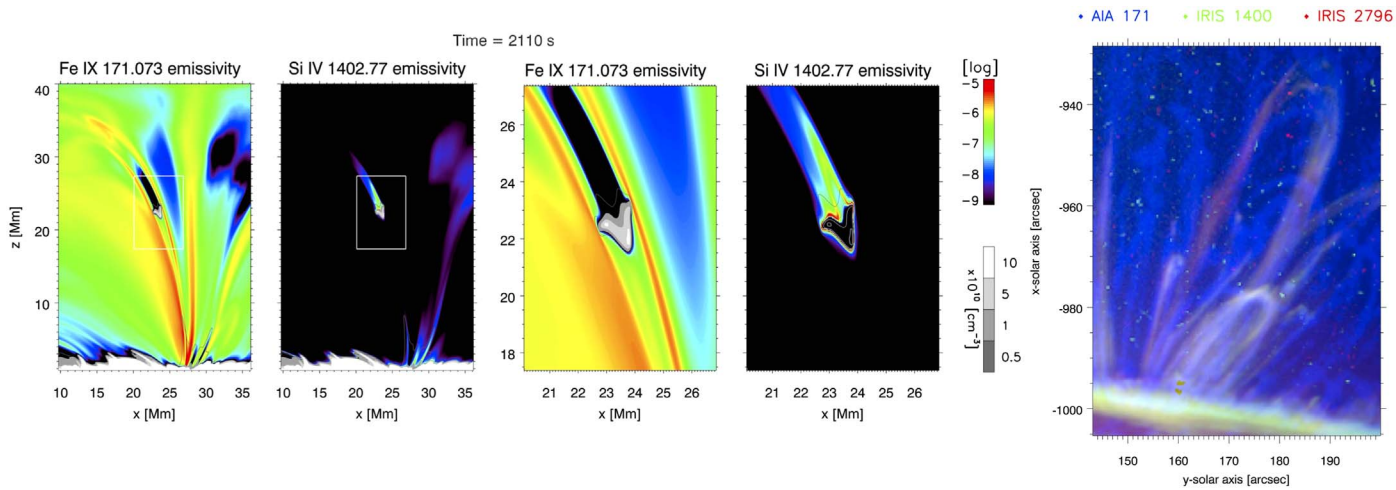

Figure 5. The EUV and UV morphology of coronal rain. The first two panels show the forward modeling in the Fe IX 171.073 and Si IV 1403.77 Å lines of the simulated region shown in Figure 2. The emissivities for both lines are overlaid with isocontours of the density in gray scale. The next two panels show a zoomed-in region corresponding to the white square inset. For better visualization, the isocontours of density are not filled in the Si IV map. The panel on the right shows a combined color image of an active region observed off-limb with AIA 171 (blue), IRIS 1400 (green), and IRIS 2796 (red). The image corresponds to the average over a time duration of 20 minutes. Multi-Gaussian normalization has been applied to AIA 171 to enhance the coronal structures (Morgan & Druckmüller 2014). The accompanying animation only corresponds to the four-panel set on the left and shows the evolution of the forward-modeled loop for the same duration as in Figure 2. The real-time animation duration is 14 s.

(An animation of this figure is available.)

the observation. In our simulation, the tail is seen to increase its emission to equal levels compared to the envelope when the clump is just 2 Mm above the chromosphere. On the other hand, the strongly compressed downstream region starts to emit strongly at this time, reaching an emission peak at the time of impact lasting under 10 s. These short bursts of UV intensity can explain the so-called "IRIS pearls" (Kleint et al. 2014). Following the impact of the rain clump, a rebound shock is produced, leading to partial reheating of the loop.

4. Discussion and Conclusions

In this work, we have conducted 2.5D rMHD simulations with the *Bifrost* code and analyzed coronal rain self-consistently forming in a coronal loop. Recently, Kohutova et al. (2020) analyzed for the first time coronal rain self-consistently generated in a 3D rMHD simulation with *Bifrost*. The 2.5D rMHD setup of the present investigation allows a much higher spatial resolution and larger numerical box size, which permits the investigation of coronal rain formation in commonly seen long loops at high enough resolution for proper comparison with observations.

The magnetoconvective motions and subsequent Joule heating lead to strongly stratified heating with an apex-to-footpoint ratio below 0.1, on average, and footpoint heating asymmetry below 3, satisfying the theoretical prediction for TNE onset by Klimchuk & Luna (2019). The excursion seen above 3 for the heating asymmetry corresponds to the time of impact of the rain and is likely produced by it. The TNE should be largely insensitive to such excursions that occur on timescales below the freefall time of the loop. In our simulation, magnetic reconnection is continuously changing the connectivity of the field lines. In this setup, coronal rain forms in a newly closed loop subject to strongly stratified heating. The rain event is characterized by a dense, chromospheric head with sizes of 100–200 km, comparable to the observed clumps in Hα (Antolin & Rouppe van der Voort 2012; Jing et al. 2016). The clump is surrounded by a very thin envelope that strongly emits in the far-UV (as in the Si IV 1402 line), known as the CCTR, matching very well with observational estimates (Antolin et al. 2015). It is further characterized by a warm tail (at TR temperatures) that can span tens of megameters and emits in the UV and EUV (including Fe IX 171). Strong UV and EUV emission is also produced ahead of the clump due to the strong compression. Overall, a plume-like feature is obtained, resembling the structures often seen rooted in the umbrae/penumbrae of sunspots and along which supersonic downflows associated with coronal rain are often observed (Dere 1982; Nelson et al. 2020). The impact on the lower atmosphere leads to very short and bright UV bursts, providing an explanation for similar phenomena seen with IRIS (Kleint et al. 2014). Following the impact, a strong rebound shock is seen to partially reheat the loop.

Although our results suggest that current ground-based instrumentation is resolving the rain size distribution, we cannot discard the possibility that 3D effects (such as instabilities and associated turbulence) may enhance the population at the lowest spatial scales.

The formation of coronal rain is seen to advect the field lines radially inward toward the loop axis, increasing the magnetic field strength by a few Gauss over the width of the rain. This process is due to the catastrophic pressure loss produced by the radiative losses that drive the TI and is not a localized effect. This process affects most of the loop due to flux freezing in a low-β environment and the pressure balance condition. We therefore obtain a well-defined strand-shaped entity with no further magnetic substructure. Therefore, TI generates what could be considered as a fundamental magnetic strand in the coronal loop with a width of a few hundred kilometers. A small TR between the corona and warmer material at TR temperatures forms at both sides of the clump's tail, leading to thin strands emitting in the Fe IV 171 line. Assuming axisymmetry around the loop, we would expect a thin envelope emitting in the EUV around the thermally unstable loop, both ahead and at the wake of the rain clump. These results therefore provide a

link between the rain strands observed in the visible range (with, e.g., the SST; Antolin & Rouppe van der Voort 2012), with the EUV strands observed with *Hi-C* (Williams et al. 2020). The physical process determining the size of these structures may be the magnetoconvective motions and associated currents (Martínez-Sykora et al. 2018). Furthermore, these results strongly suggest that TI may play a major role in the observed filamentary structure of the solar corona in TR temperatures (e.g., Ugarte-Urra et al. 2009).

On the dynamics side, we see the densest (and coolest) part of the rain falling faster, in agreement with the numerical prediction of Oliver et al. (2014). Significant shear flows are also observed, whose influence on the dynamics and morphology is also expected to play a dominant role (Fang et al. 2015).

Magnetic strands generated by TI are also expected in the observed cold filaments within galaxy clusters (Sharma et al. 2010). In this case, the filamentary structure is also imprinted on the X-ray-emitting plasma characteristic of the hot intracluster medium. The coronal rain case may present a relevant difference regarding the combination of the magnetic topology and the dynamics. Although the coronal rain is tracing the magnetic field at all times, at any one time, the observed inclination of the rain strand can be misaligned with the magnetic topology because of the different velocities across the clump. A similar effect has been predicted in prominences (Claes et al. 2020). Caution must be taken when inferring field direction based on instantaneous snapshots of coronal rain, since it is its motion that indicates the field direction.

We would like to thank the anonymous referee for the valuable contribution during the reviewing process of this manuscript. This work was supported by computational time granted from the Greek Research & Technology Network (GRNET) in the National HPC facility—ARIS. Part of the numerical computations were also carried out on the Cray XC50 at the Center for Computational Astrophysics, NAOJ. P. A. acknowledges funding from his STFC Ernest Rutherford Fellowship (No. ST/R004285/2).

We gratefully acknowledge support by NASA grants 80NSSC18K1285, 80NSSC20K1272, 80NSSC21K0737, and 80NSSC21K1684 and contract NNG09FA40C (IRIS). The simulations have been run on the Pleiades cluster through computing projects s1061, s2601, and s8305 from the High End Computing (HEC) division of NASA. To analyze the data, we have used IDL. This research is also supported by the Research Council of Norway through its Centres of Excellence scheme, project No. 262622, and through grants of computing time from the Programme for Supercomputing. Data are courtesy of IRIS. IRIS is a NASA small explorer mission developed and operated by LMSAL with mission operations executed at NASA Ames Research Center and major contributions to downlink communications funded by ESA and the Norwegian Space Centre.

ORCID iDs

Patrick Antolin https://orcid.org/0000-0003-1529-4681
Juan Martínez-Sykora https://orcid.org/0000-0002-0333-5717
Seray Şahin https://orcid.org/0000-0003-3469-236X

References

Antolin, P. 2020, PPCF, 62, 014016
Antolin, P., & Rouppe van der Voort, L. 2012, ApJ, 745, 152
Antolin, P., Vissers, G., Pereira, T. M. D., Rouppe van der Voort, L., & Scullion, E. 2015, ApJ, 806, 81
Aschwanden, M. J., & Peter, H. 2017, ApJ, 840, 4
Auchère, F., Froment, C., Soubrié, E., et al. 2018, ApJ, 853, 176
Brooks, D. H., Warren, H. P., Ugarte-Urra, I., & Winebarger, A. R. 2013, ApJL, 772, L19
Brynildsen, N., Maltby, P., Kjeldseth-Moe, O., & Wilhelm, K. 2001, ApJL, 552, L77
Carlsson, M., & Leenaarts, J. 2012, A&A, 539, A39
Chen, H., Tian, H., Li, L., et al. 2021, A&A, arXiv:2112.01354
Chitta, L. P., Peter, H., & Young, P. R. 2016, A&A, 587, A20
Claes, N., & Keppens, R. 2021, SoPh, 296, 143
Claes, N., Keppens, R., & Xia, C. 2020, A&A, 636, A112
De Groof, A., Berghmans, D., van Driel-Gesztelyi, L., & Poedts, S. 2004, A&A, 415, 1141
Del Zanna, G., Dere, K. P., Young, P. R., & Landi, E. 2021, ApJ, 909, 38
Dere, K. P. 1982, SoPh, 77, 77
Fang, X., Xia, C., Keppens, R., & Van Doorsselaere, T. 2015, ApJ, 807, 142
Field, G. B. 1965, ApJ, 142, 531
Froment, C., Auchère, F., Aulanier, G., et al. 2017, ApJ, 835, 272
Froment, C., Auchère, F., Bocchialini, K., et al. 2015, ApJ, 807, 158
Gudiksen, B. V., & Nordlund, Å. 2005, ApJ, 618, 1020
Gudiksen, B. V., Carlsson, M., Hansteen, V. H., et al. 2011, A&A, 531, A154
Hansteen, V. H., Hara, H., De Pontieu, B., & Carlsson, M. 2010, ApJ, 718, 1070
Hayek, W., Asplund, M., Carlsson, M., et al. 2010, A&A, 517, A49
Jing, J., Xu, Y., Cao, W., et al. 2016, NatSR, 6, 24319
Kanella, C., & Gudiksen, B. V. 2019, A&A, 621, A95
Kjeldseth-Moe, O., & Brekke, P. 1998, SoPh, 182, 73
Kleint, L., Antolin, P., Tian, H., et al. 2014, ApJL, 789, L42
Klimchuk, J. A., & Luna, M. 2019, ApJ, 884, 68
Kohutova, P., Antolin, P., Popovas, A., Szydlarski, M., & Hansteen, V. H. 2020, A&A, 639, A20
Li, L., Zhang, J., Peter, H., et al. 2018, ApJL, 864, L4
Li, X., Keppens, R., & Zhou, Y. 2021, arXiv:2112.02702
Martínez-Gómez, D., Oliver, R., Khomenko, E., & Collados, M. 2020, A&A, 634, A36
Martínez-Sykora, J., De Pontieu, B., Carlsson, M., et al. 2017, ApJ, 847, 36
Martínez-Sykora, J., De Pontieu, B., De Moortel, I., Hansteen, V. H., & Carlsson, M. 2018, ApJ, 860, 116
Mason, E. I., Antiochos, S. K., & Viall, N. M. 2019, ApJL, 874, L33
Morgan, H., & Druckmüller, M. 2014, SoPh, 289, 2945
Moschou, S. P., Keppens, R., Xia, C., & Fang, X. 2015, AdSpR, 56, 2738
Nelson, C. J., Krishna Prasad, S., & Mathioudakis, M. 2020, A&A, 636, A35
Oliver, R., Soler, R., Terradas, J., Zaqarashvili, T. V., & Khodachenko, M. L. 2014, ApJ, 784, 21
Schad, T. A., Penn, M. J., Lin, H., & Judge, P. G. 2016, ApJ, 833, 5
Schrijver, C. J. 2001, SoPh, 198, 325
Scullion, E., Rouppe van der Voort, L., Antolin, P., et al. 2016, ApJ, 833, 184
Sharma, P., Parrish, I. J., & Quataert, E. 2010, ApJ, 720, 652
Skartlien, R. 2000, ApJ, 536, 465
Straus, T., Fleck, B., & Andretta, V. 2015, A&A, 582, A116
Ugarte-Urra, I., Warren, H. P., & Brooks, D. H. 2009, ApJ, 695, 642
Williams, T., Walsh, R. W., Winebarger, A. R., et al. 2020, ApJ, 892, 134
Xia, C., Keppens, R., & Fang, X. 2017, A&A, 603, A42